APPENDIX A

An Automated SAR Measurement System for Compliance Testing of Personal Wireless Devices

Q. Yu, M. Aronsson, D. Wu, and O.P. Gandhi

Department of Electrical Engineering
University of Utah
Salt Lake City, Utah 84112

Abstract

An automated SAR measurement system has been developed for compliance testing of personal wireless devices. The setup uses a 3-D stepper motor system to move a Narda Model 8021 E-field probe to measure the SAR distribution inside a head-shaped tissue-simulant phantom near the radiating device. The head and neck part of the model is made of an outer shell of 5-7 mm thickness of epoxy laced with KCl solution for losses. This and the upper part of the torso are filled with a liquid with measured electrical properties (dielectric constant and conductivity) that are close to those for the brain at the center frequencies of interest (840 and 1900 MHz). The implantable E-field probe is calibrated against FDTD-calculated SAR variations for a slab model at AMPS (840 MHz) and PCS (1900 MHz) frequencies and is checked to have good isotropic characteristics (±0.23 dB) and a wide dynamic range (1 mW/kg - 10 W/kg). The system is validated using a 223 mm diameter sphere model. Several commercial telephones with different types of antennas have been measured for 1-g SAR using the system, and excellent agreement (within ± 1dB) with numerical results has been obtained.

Submitted to IEEE Transactions on Electromagnetic Compatibility, March 1998.

I. Introduction

The use of cellular telephones and mobile wireless communication systems has increased dramatically during the past few years. Meanwhile, there is public concern for safety of RF exposure from these devices. Since the RF exposure is quantified by the mass-normalized rate of electromagnetic energy absorption or the Specific Absorption Rate (SAR), the U.S. Federal Communications Commission (FCC) requires that the SAR values of new personal wireless devices must meet the prescribed RF safety guidelines [1]. Furthermore, since electromagnetic energy absorbed by the human head depends to a large extent on the antenna used for the personal wireless devices [2], knowledge of SAR distributions in the human head can also help the industry to design better antennas to improve the performance of the wireless transceivers. In this regard we should note that 30-65 percent of the power radiated by the helix-monopole antennas used today is wasted by absorption in the human head and hand [2] and this could be reduced greatly.

Recent dosimetric studies on the RF exposure to the human body from personal wireless devices have been carried out by both numerical simulation [3-5] and experimental measurements [6, 7]. Numerical methods using millimeter resolution anatomically based human body models and CAD files could simulate the human body and the cellular phones in much more detail, respectively, thus providing highly accurate information about the electromagnetic coupling of the radiating device to the human body [8], but they generally require increasing computational resources (memory and computation time) for just one test condition of the device [8]. To alleviate this problem, use of the expanding grid FDTD method [9] together with the use of the truncated models of the head [10] has resulted in savings of memory requirements by factors in excess of

20 making it possible to compute the high resolution SAR distributions using workstations instead of parallel computers [11]. Nevertheless, if a device is to be tested for several orientations relative to the head, an easy, fast experimental procedure with validated accuracy and repeatability is of interest. The difficulties encountered by the experimental techniques lie mainly in two aspects: the construction of a validated phantom model that could accurately simulate electromagnetic coupling to the human head at least in the context of peak 1-g SAR for compliance testing required by FCC [1], and a miniature E-field probe which has a wide dynamic range and good isotropy and is calibrated properly at the AMPS (840 MHz) and PCS (1900 MHz) frequencies. In this paper, we will present an automated SAR measurement system developed for compliance testing at both 840 and 1900 MHz. The system is fully automated by a 3D stepper motor system controlled by a computer, with a miniature implantable E-field probe that is used to determine spatial SAR variations. The head and neck part of the phantom model is made of an outer shell of 5-7 mm thickness of epoxy laced with KCl solution for losses. This and the upper part of the torso are filled with a liquid with measured electrical properties (dielectric constant and conductivity) close to the average properties of the brain for white and gray matters at the center frequency of interest. Ten commercial telephones, five each at 840 and 1900 MHz, with different types of antennas have been measured for peak 1-g SARs using this system. Agreement with the FDTD-calculated values using the anatomically-based model of a male adult is within ± 1dB.

II. Experimental Setup and Measurements

A. The Specific Absorption Rate (SAR)

The RF exposure to human body from wireless devices can be quantified by the Specific Absorption Rate (SAR) which measures the rate at which electromagnetic energy is absorbed by the exposed tissues. It can be expressed as follows[12]:

$$SAR = \sigma|E_i|^2/\rho \qquad (1)$$

where σ is the conductivity of the tissue, ρ is the mass density and E_i is the *rms* value of the internal electric field. The unit of SAR is Watts per kilogram (W/kg).

Since the SAR is proportional to the square of the local electric field, it can be determined by measuring the electric field inside the exposed tissue-simulant volume. Two SAR values are required for compliance testing [1]: the whole body average SAR, which is the ratio of the total power absorbed by the exposed body to its mass, should be below 0.08 W/kg, and the spatial peak SAR, as averaged over any of 1-g of tissue, which should not exceed 1.6 W/kg. Since most mobile telephones have an output power below 1 W, the whole body average SAR is well below the limit of 0.08 W/kg. The peak 1-g SAR, however, may exceed the safety limit for devices even with fairly low output power [2]. This therefore, needs to be accurately measured for compliance testing.

B. The Experimental Setup

The diagram of the experimental setup is shown in Fig. 1. A commercial Narda Model 8021 E-field probe is mounted on a computer-controlled 3D stepper motor system (Arrick Robotics MD-2A) to determine the SAR distributions inside the phantom tissue.

The positioning repeatability of the stepper motor system is within ±0.1 mm. Outputs from the three channels of the E-field probe are dc voltages, the sum of which is proportional to $|E_i|^2$ as well as SAR through Eq. (1). The dc voltages are read by three HP 34401A multimeters and sent to the computer via HPIB interface. The setup is properly grounded to reduce noise due to EMI.

The internal surface of the phantom is pre-scanned with a high resolution (2x2 mm) so that the computer knows how far it can move the probe in the vertical direction (z) at each horizontal position (x, y) without breaking the probe. A special program is written to scan the phantom surface. Before scanning, a thin copper film is first tightly taped to the internal surface of the phantom, then a metal rod with the same shape and diameter as the E-field probe is moved by the stepper motor system on the programmed path to detect the surface, when the metal rod's tip touches the surface, an electrical signal is sent to the computer, the computer stops the stepper motor and records the position (x, y, z). Since the positions of the stepper motor system and the phantom are relatively stable, pre-scanning of the phantom surface is needed only once for each phantom model.

The compliance testing procedure includes two steps: a coarser sampling with a step size of 8.0 mm is done in the first instance to locate the peak SAR region. The coarser scan area is 4.8 cm x 8.0 cm, with each sampling close to the phantom surface. The peak SAR region is then sampled with a finer step size of 2.0 mm on a 3D grid over a 1 cm^3 volume cube, a total of 5 x 5 x 5 points are measured. The fine scan data are processed by the computer to give the peak 1-g SAR. The whole testing procedure takes about 20 minutes with coarser and finer sampling steps taking about 10 minutes each, so

the measurement can be finished within the battery charge life of most personal wireless devices.

C. The Phantom Model

As shown in Fig. 2, the phantom model used in the setup has dimensions similar to the upper parts of the human body. The head and neck part of the model is made of an outer shell of 5-7 mm thickness of epoxy laced with KCl solution for losses. This and the upper part of the torso are filled with a liquid with measured electrical properties (dielectric constant and conductivity) close to the average properties of the brain for white and gray matters at the center frequency of interest. Table 1 shows the desired tissue properties [13] and the measured electrical properties of the skull- and brain-simulant materials at 840 and 1900 MHz. The head and neck region of the phantom is filled with brain simulating liquid materials of compositions given in Table 2. The model also has shoulders and chest, which are filled with a semi-solid composition of water, salt, polyethylene powder, and a gelling agent TX151 that simulates the dielectric properties equivalent to those of two-thirds muscle. The same material is used to fill a thin surgical rubber glove to create the shape of the hand. As shown in Fig. 2, the "hand " thus created is used to hold the cellular telephone which is positioned against the phantom head along the line connecting the ear canal and the mouth of the phantom. This is done in order to load the handset similar to the dielectric loading provided by the hand in actual use of a hand-held wireless device.

Two different fluids of compositions given in Table 2 are used to simulate the average dielectric properties of the brain at 840 and 1900 MHz. The clear fluid used at

840 MHz is a composition of water, sugar, salt, and a gelling agent HEC proposed by Hartsgrave et al [14]. Even without salt, this composition has an electrical conductivity σ = 1.65 S/m which is considerably higher than σ = 1.29 S/m needed to simulate the average properties for the brain at 1900 MHz [13]. Thus we have developed another liquid brain simulating material for SAR measurements at 1900 MHz. The composition of this material is also given in Table 2. The dielectric properties of this material were measured using a HP 85070B dielectric probe measurement system and are given in Table 2. The brain-simulant composition for use at 1900 MHz has shown a very good long term stability (Table 3) when it is properly sealed after measurements to minimize the vaporization of water.

D. The E-field Probe

The non-perturbing implantable E-field probe used in the setup was originally developed by Bassen et al [15] and is now manufactured by L3/Narda Microwave Corporation, Hauppauge, New York as Model 8021 E-field probe. In the probe, three orthogonal miniature dipoles are placed on a triangular beam substrate. Each dipole is loaded with a small Schottky diode and connected to the external circuitry by high resistance (2 MΩ $\pm$ 40%) leads to reduce secondary pickups. The entire structure is then encapsulated with a low dielectric constant insulating material. The probe thus constructed has a very small (4 mm) diameter, which results in a relatively small perturbation of the internal electric field.

Test for Square Law Region

It is necessary to operate the E-field probe in the square law region for each of the diodes so that the sum of the dc voltage outputs from the three dipoles is proportional to the square of the internal electric field ($|E_i|^2$). Fortunately the personal wireless devices induce SARs that are generally less than 5-6 W/kg even for closest locations of the head [2]. For compliance testing it is therefore necessary that the E-field probe be checked for square law behavior for SARs up to such values that are likely to be encountered. Such a test may be conducted using a canonical lossy body such as a rectangular box or a sphere irradiated by a dipole. By varying the radiated power of the dipole, the output of the probe should increase linearly with the applied power for each of the test locations.

Shown in Figs. 3a, 3b are the results of the tests performed to check the square law behavior of the E-field probe used in our setup at 840 and 1900 MHz, respectively. For these measurements we have used a rectangular box of dimensions 30 x 15 x 50 cm that was irradiated by the corresponding half wave dipoles with different amounts of radiated powers from 200-800 mW. Since the dc voltage outputs of the probe are fairly similar when normalized to a radiated power of 100 mW, the square law behavior is demonstrated and an output voltage that is proportional to $|E_i|^2$ is obtained within $\pm$ 3 percent.

Test for Isotropy of the probe

Another important characteristic of the probe that affects the measurement accuracy is its isotropy. Since the orientation of the induced electric field is generally unknown, the E-field probe should be relatively isotropic in its response to the orientation

of the E-field. Shown in Figs. 4a, 4b are the test results of the E-field probe used in our setup at 840 and 1900 MHz, respectively. The previously described box phantom of dimensions 30 x 15 x 50 cm along x, y and z dimensions, respectively, was also used for these measurements. This phantom was filled to a depth of 15 cm with brain-simulant materials (Table 2). The E-field probe was rotated around its axis from 0 to 360° in incremental steps of 60°. An isotropy of less than ±0.23 dB(±5.5%) was observed for this E-field probe both at 840 and 1900 MHz.

Calibration of the E-field Probe

Since the voltage output of the E-field probe is proportional to the square of the internal electric field ($|E_i|^2$), from the definition of SAR (Eq. 1), the SAR is therefore proportional to the voltage output of the E-field probe by a proportionality constant C. The constant C is defined as the calibration factor, and is frequency and material dependent. It is measured to calibrate the probe at the various frequencies of interest using the appropriate tissue-simulating materials for the respective frequencies.

Canonical geometries such as waveguides, rectangular slabs and layered or homogeneous spheres have in the past been used for the calibration of the implantable E-field probe [16-18]. Since the Finite Difference Time Domain (FDTD) has been carefully validated to solve electromagnetic problems for a variety of geometries [19, 20], we were able to calibrate the Narda E-field probe by comparing the measured variations of the probe voltage ($\approx |E_i|^2$) against the FDTD-calculated variations of SARs for a box phantom of dimensions 30 x 15 x 50 cm used previously for the data given in Figs. 3 and 4, respectively. For these measurements we placed the nominal half-wave dipoles of lengths

178 mm and 77 mm at 840 and 1900 MHz, respectively, at several distances d (see inserts of Figs. 5a, 5b and 6a, 6b) from the outer surface of the acrylic (ε_r = 2.56) box of thickness 6.55 mm. Shown in Figs. 5a, 5b and 6a, 6b are the comparisons between the experimentally measured and FDTD-calculated variations of the SAR distributions for this box phantom. Since there are excellent agreements between the calculated SARs and the measured variations of the voltage output of the E-field probe for four different separations d of the half wave dipoles at each of the two frequencies, it is possible to calculate the calibration factors at the respective frequencies. For the Narda Model 8021 E-field probe used in our setup, the calibration factors are determined to be 0.49 and 0.84 (mW/kg)/μV at 840 and 1900 MHz, respectively

III. Experimental Results: Canonical Problems

To further validate the system, it has been used to measure the peak 1-g SAR for the above-mentioned box phantom and a glass sphere model of thickness 5 mm, external diameter = 223 mm and dielectric constant ε_r = 4.0. This sphere model is once again filled with the corresponding brain-simulant fluids of compositions given in Table 2. Shown in Figs. 7a, 7b and 8a, 8b are the measured and FDTD-calculated SAR distributions inside the sphere for various separations d between the dipole and the sphere (see insert for Figs. 7, 8). Comparison of the measured and FDTD-calculated peak 1-g SARs for both phantom geometries are given in Table 4 and 5, respectively. As can be seen, the agreement between experimental measurement and numerical simulation is excellent and generally within ± 10 percent for both rectangular and spherical phantoms.

Since the dipole sensors of the Narda Model 8021 E-field probe used for SAR measurements are recessed about 4 mm from the tip of the probe, it is necessary to use an extrapolation subroutine to obtain the SARs at the internal surface for both of these phantoms as these are generally the highest and contribute the most to the peak 1-g SAR. A second order polynomial obtained by using the least mean square error method to fit the measured data was used to extrapolate the SARs to the phantom surface in our measurements. As shown in Figs. 5a, 6a, the results are satisfactory compared to the FDTD simulations.

IV. SAR Measurements for Cellular Telephones

The automated setup shown in Fig. 2 has been used for the testing of ten commercial personal wireless devices five each at 835 and 1900 MHz, respectively. Given in Table 6 is the comparison of the numerical and measured peak 1-g SARs for these devices using our experimental phantom model and the FDTD-based numerical procedure used for calculations of SAR distributions for an anatomically-based model of the head of an adult male. The measured and calculated SARs for the ten telephones which have quite different operational modes (TDMA, CDMA, etc.) and antenna structures (helical, monopole, or helix-monopole) vary from 0.13 to 5.41 W/kg. Even though widely different peak 1 g SARs are obtained because of the variety of antennas and handsets, agreement between the calculated and the measured data is excellent and generally within ± 20% (± 1 dB). This is particularly remarkable since an MRI-derived, 16-tissue anatomically-based model of the adult human head is used for FDTD calculations and a relatively simplistic two tissue phantom model is used for experimental

peak 1-g SAR measurements. It is interesting to note that even though the dielectric properties of the external shell (Fig. 2) are not as high as for human skull (see Table 1), the peak 1-g SARs obtained with this experimental phantom model are quite accurate.

V. Conclusions

An automated SAR measurement system has been developed with a dynamic range (1mW/kg to 10W/kg) suitable for the compliance testing of personal wireless devices. With a miniature Narda E-field probe, the system provides accurate measurements at 840 MHz as well as 1900 MHz. Besides the peak 1-g SAR, the system also gives the SAR distributions for any radiating device, thus providing information for better antenna design.

The E-field probe is a crucial part of the system. The accuracy of measurement can be further improved by using probes with still smaller size, better isotropy and less sensor offset from the tip. The dielectric properties of the various tissues for a heterogeneous phantom have been well established and recognized, however, since the SAR measurements are very sensitive to the geometric shape and size of the phantom model, it would be desirable to standardize the phantom model for consistent and comparable testing results. Before a phantom model can be considered to be acceptable, it should be validated, as in Table 6, for accuracy relative to realistic anatomically-based models of the human body.

Acknowledgment

The authors gratefully acknowledge many helpful discussions and the FDTD calculations provided by Drs. Gianluca Lazzi and Adam Tinniswood.

References

1. FCC 96-326, "Guidelines for evaluating the environmental effects of radio frequency radiation," August 1, 1996, Federal Communications Commission, Washington, DC, 20554.

2. O. P. Gandhi, G. Lazzi, and C. M. Furse, "Electromagnetic absorption in the human head and neck for mobile telephones at 835 and 1900 MHz," *IEEE Trans. Microwave Theory Tech.*, Vol. 44, pp. 1884-1897, 1996.

3. P. J. Dimbylow and S. M. Mann, "SAR calculations in an anatomically based realistic model of the head for mobile communication transceivers at 900 MHz and 1.8 GHz," *Physics in Medicine and Biology*, Vol. 39, pp. 1537-1553, 1994.

4. O. P. Gandhi and J. Y. Chen, "Electromagnetic absorption in the human head from experimental 6-GHz transceivers," *IEEE Trans. Electromag. Compat.,* Vol. 37, pp. 547-558, 1995.

5. M. A. Jensen and Y. Rahmat-Samii, "EM interaction in handset antennas and a human in personal communications," *Proc. IEEE*, Vol. 83, pp. 7-17, 1995.

6. Q. Balzano, O. Garay, and T. J. Manning, Jr., "Electromagnetic energy exposure of simulated users of portable cellular telephones," *IEEE Trans. Veh. Technol.*, Vol. 44, pp. 390-403, 1995.

7. T. Schmid, O. Egger, and N. Kuster, "Automated E-field scanning system for dosimetric assessments," *IEEE Trans. Microwave Theory Tech.*, Vol. 44, pp. 105-113, 1996.

8. A. D. Tinniswood, C. M. Furse and O. P. Gandhi, "Computations of SAR distributions for two anatomically-based models of the human head using CAD files of commercial telephones and the parallelized FDTD code," *IEEE Trans. Antennas Propagat.*, Vol. 46, 1998.

9. B. Q. Gao and O. P. Gandhi, "An expanding-grid algorithm for the finite-difference time-domain method," *IEEE Trans. Electromag. Compat.*, Vol. 34, pp. 277-283, 1992.

10. G. Lazzi and O. P. Gandhi, "Realistically tilted and truncated anatomically-based models of the human head for dosimetry of mobile telephones," *IEEE Trans. on Electromag. Compat.*, vol. 39, pp. 55-61, 1997.

11. A. Tinniswood, G. Lazzi and O. P. Gandhi, "The use of the expanding grid FDTD method for simulation of CAD-derived personal wireless devices," Submitted to *IEEE Trans. Microwave Theory Tech.*.

12. M. A. Stuchly and S. S. Stuchly, "Experimental radio and microwave dosimetry," in *Handbook of Biological Effects of Electromagnetic Fields*, second edition, edited by C. Polk and E. Postow, CRC Press, Baca Raton, Florida, pp. 295-336, 1996.

13. C. Gabriel, "Compilation of the Dielectric properties of body tissues at RF and microwave frequencies," U.S. Air Force Armstrong Laboratory, Report AL/OE-TR-1996-0037, Brooks Air Force Base, Texas, 78235, June 1996.

14. G. Hartsgrave, A. Kraszewski and A. Surowiec, "Simulated biological materials for electromagnetic absorption studies," *Bioelectromagnetics*, Vol. 8, pp. 29-36, 1987.

15. H. I. Bassen and G. S. Smith, "Electric field probes — a review," *IEEE Trans. Antennas Propagat.*, Vol. 3, pp710-718, Sept., 1983.

16. D. Hill, "Waveguide techniques for the calibration of miniature electric field probes for use in microwave bioeffects studies," *IEEE Trans. Theory Tech.*, Vol. 30, pp. 92-94, 1982.

17. N. Kuster and Q. Balzano, "Energy absorption mechanism by biological bodies in the near field of dipole antennas above 300 MHz," *IEEE Trans. Veh. Technol.*, Vol. 41, pp. 17-23, 1992.

18. M. A. Stuchly, S. S. Stuchly, and A. Kraszewski, "Implantable electric field probes — some performance characteristics," *IEEE Trans. Biomed. Eng.*, Vol. 31, pp. 526-531, 1984.

19. A. Taflove, K. R. Umashankar, T. G. Jurgens, "Validation of FDTD modeling of the radar cross section of three-dimensional structures spanning up to nine wavelengths," *IEEE Trans. Antennas and Propagat.*, pp. 662-666, 1985.

20. C. M. Furse, Q. Yu and O. P. Gandhi, "Validation of the Finite-Difference Time-Domain method for near-field bioelectromagnetic simulations," *Microwave and Optical Technology Letters*, Vol. 16, pp.341-345, 1997.

Figure Captions

Figure 1: Block diagram of the experimental setup of the automated SAR measurement system.

Figure 2: Phantom model used in the automated SAR measurement system.

Figure 3a: Test for square-law behavior at 840 MHz: Variation of the output voltage (proportional to $|E_i|^2$) for different radiated powers normalized to 0.1 W.

Figure 3b: Test for square-law behavior at 1900 MHz: Variation of the output voltage (proportional to $|E_i|^2$) for different radiated powers normalized to 0.1 W.

Figure 4a: Test for isotropy: The model shown in Figure 2 was used with nominal half wavelength dipole radiator of length 178 mm at 840 MHz.

Figure 4b: Test for isotropy: The model shown in Figure 2 was used with nominal half wavelength dipole radiator of length 77 mm at 1900 MHz.

Figure 5a: Comparison of the calculated and measured SAR variations for a box phantom of dimensions 30 x 15 x 50 cm; 840 MHz; $\lambda/2$ dipole antenna; 0.5 W radiated power. Calibration factor for the Narda Model 8021 probe at 840 MHz = 0.49 (mW/kg)/μV. Measured for the phantom material $\varepsilon_r = 41.1$, $\sigma = 1.06$ S/m.

Figure 5b: Comparison of the calculated and measured SAR variations for a box phantom of dimensions 30 x 15 x 50 cm for a line AB parallel to the z axis at a distance y = 7 mm from the surface of the phantom material; 840 MHz; $\lambda/2$ dipole antenna; 0.5 W radiated power. Calibration factor for the Narda Model 8021 probe at 840 MHz = 0.49 (mW/kg)/μV. Measured for the phantom material $\varepsilon_r = 41.1$, $\sigma = 1.06$ S/m.

Figure 6a: Comparison of the calculated and measured SAR variations for a box phantom of dimensions 30 x 15 x 50 cm; 1900 MHz; $\lambda/2$ dipole antenna; 0.5 W radiated power. Calibration factor for the Narda Model 8021 probe at 1900 MHz = 0.84 (mW/kg)/μV. Measured for the phantom material $\varepsilon_r = 45.5$, $\sigma = 1.31$ S/m.

Figure 6b: Comparison of the calculated and measured SAR variations for a box phantom of dimensions 30 x 15 x 50 cm for a line AB parallel to the z axis at a distance y = 7 mm from the surface of the phantom material; 1900 MHz; $\lambda/2$ dipole antenna; 0.5 W radiated power. Calibration factor for the Narda Model 8021 probe at 1900 MHz = 0.84 (mW/kg)/μV. Measured for the phantom material $\varepsilon_r = 45.5$, $\sigma = 1.31$ S/m.

Figure 7a: Comparison of measured and FDTD-calculated SAR variations at 840 MHz for a glass sphere model of outer diameter 22.3 cm and thickness 5 mm. SARs normalized to a radiated power of 0.5 W. Calibration factor = 0.49 (mW/kg)/μV. Measured for the phantom material $\varepsilon_r = 41.1$, $\sigma = 1.06$ S/m.

Figure 7b: Comparison of calculated and measured SAR variations at 840 MHz for a plane at a distance of 20 mm from the lowest point on the inside of the sphere. SARs normalized to a radiated power of 0.5 W. Calibration factor = 0.49 (mW/kg)/μV. Measured for the phantom material $\varepsilon_r = 41.1$, $\sigma = 1.06$ S/m.

Figure 8a: Comparison of measured and FDTD-calculated SAR variations at 1900 MHz for a glass sphere model of outer diameter 22.3 cm and thickness 5 mm. SARs normalized to a radiated power of 0.5 W. Calibration factor = 0.84 (mW/kg)/μV. Measured for the phantom material $\varepsilon_r = 45.5$, $\sigma = 1.31$ S/m.

Figure 8b: Comparison of calculated and measured SAR variations at 1900 MHz for a plane at a distance of 20 mm from the lowest point on the inside of the sphere. SARs normalized to a radiated power of 0.5 W. Calibration factor = 0.84 (mW/kg)/μV. Measured for the phantom material $\varepsilon_r = 45.5$, $\sigma = 1.31$ S/m.

Table Captions

Table 1: The desired tissue properties and the measured electrical properties of the tissue-simulant materials for the phantom model.

Table 2: Composition used for brain equivalent materials.

Table 3: Long term stability of the phantom material at 1900 MHz.

Table 4: Box phantom: Comparison of the measured and FDTD-calculated peak 1-g SARs for four spacings each at 840 and 1900 MHz, radiated power normalized to 0.5 W.

Table 5: Sphere phantom: Comparison of the measured and FDTD-calculated peak 1-g SARs for three spacings each at 840 and 1900 MHz, radiated power normalized to 0.5 W.

Table 6: Comparison of the experimentally measured and FDTD-calculated peak 1-g SARs for ten commercial wireless devices, five each at 835 and 1900 MHz, respectively.

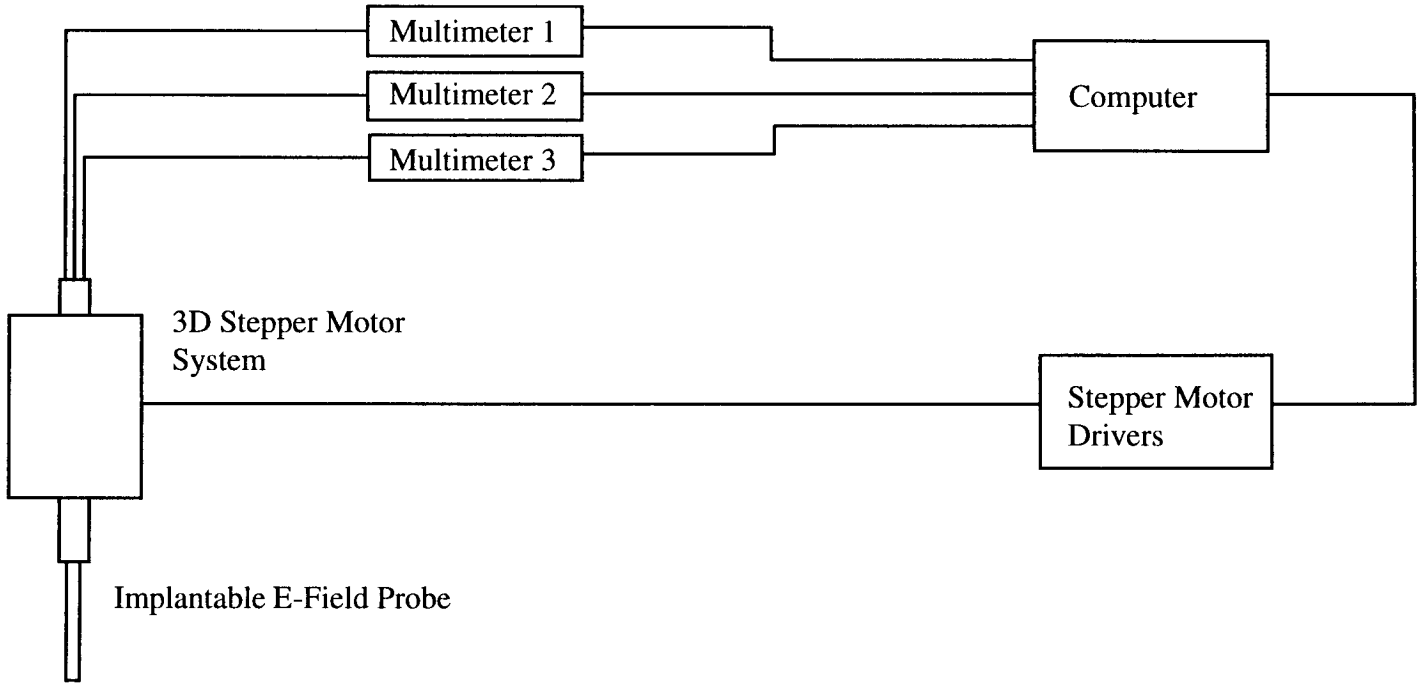

Figure 1 Block diagram of the experimental setup of the automated SAR measurement system

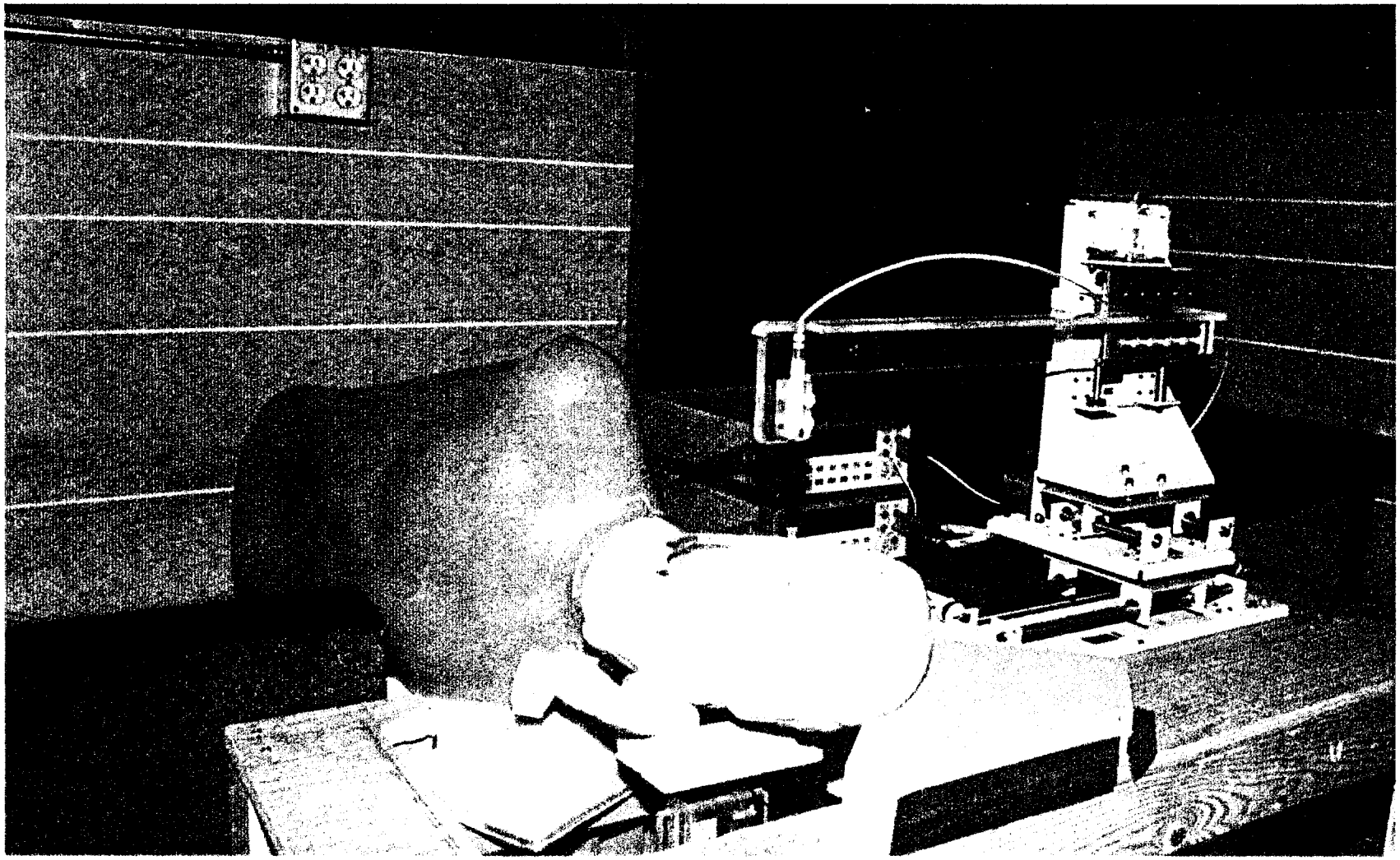

Figure 2 Phantom model used in the automated SAR measurement system.

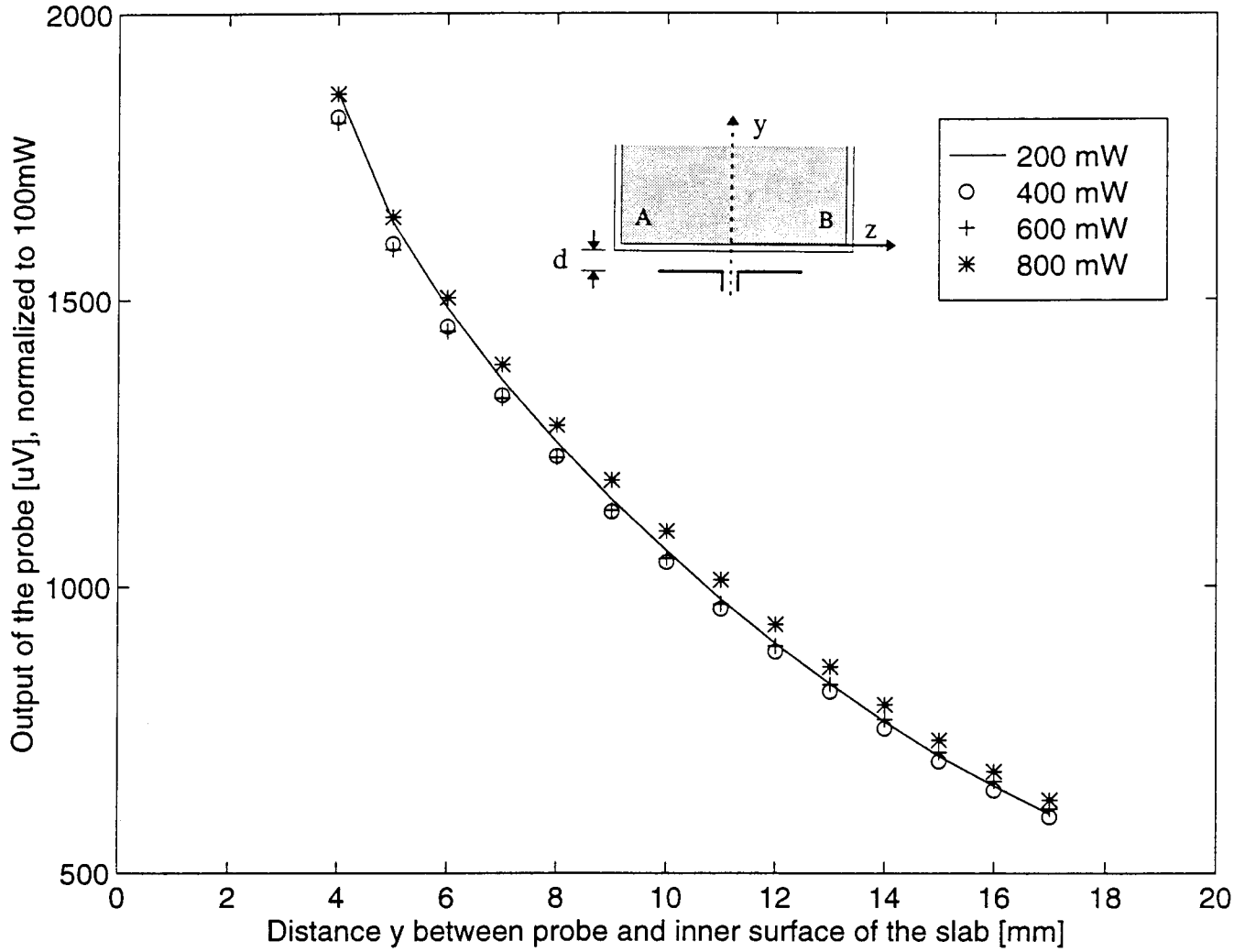

Figure 3a: Test for square-law behavior at 840 MHz: Variation of the output voltage (proportional to $|E_i|^2$) for different radiated powers normalized to 0.1 W.

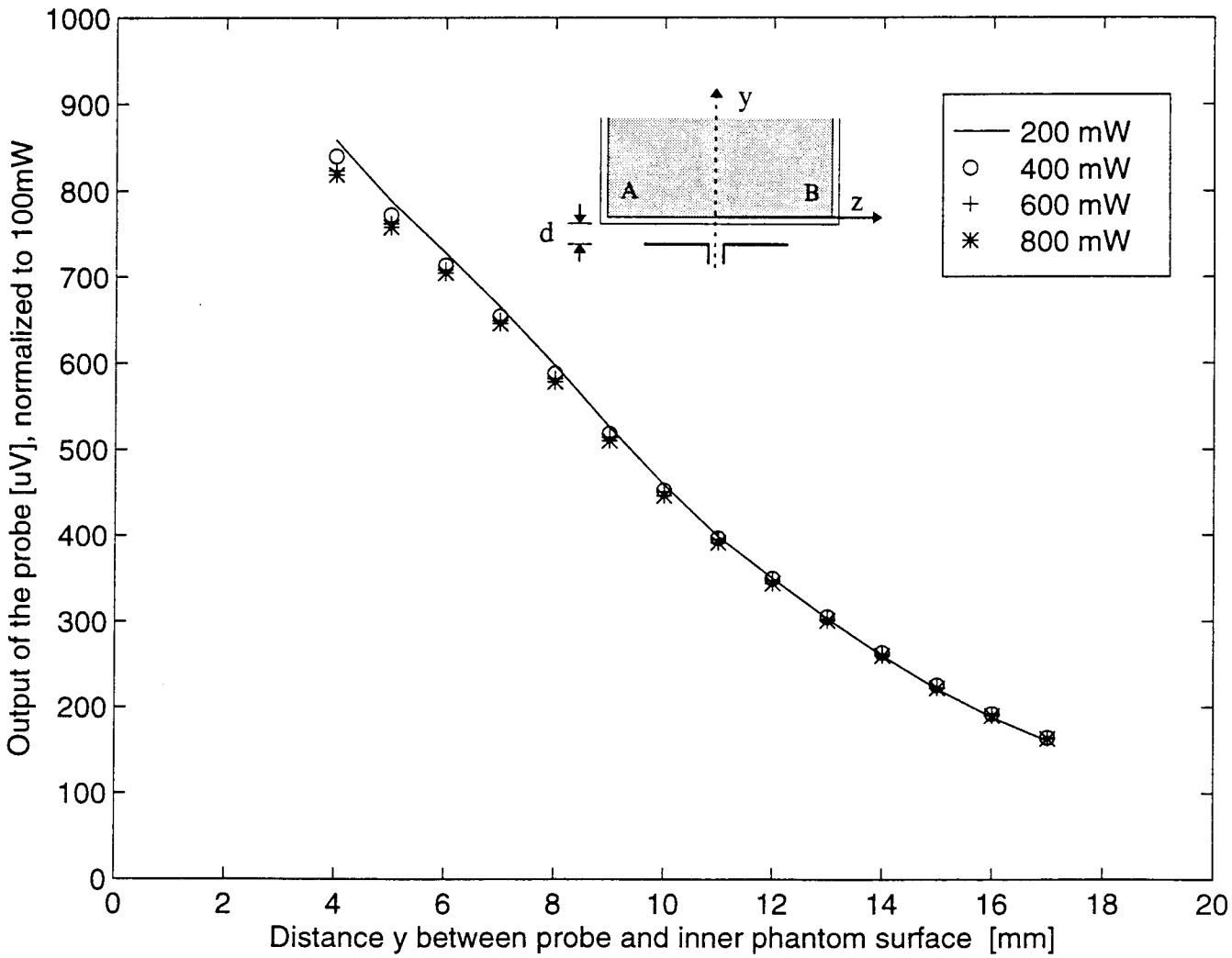

Figure 3b: Test for square-law behavior at 1900 MHz: Variation of the output voltage (proportional to $|E_i|^2$) for different radiated powers normalized to 0.1 W.

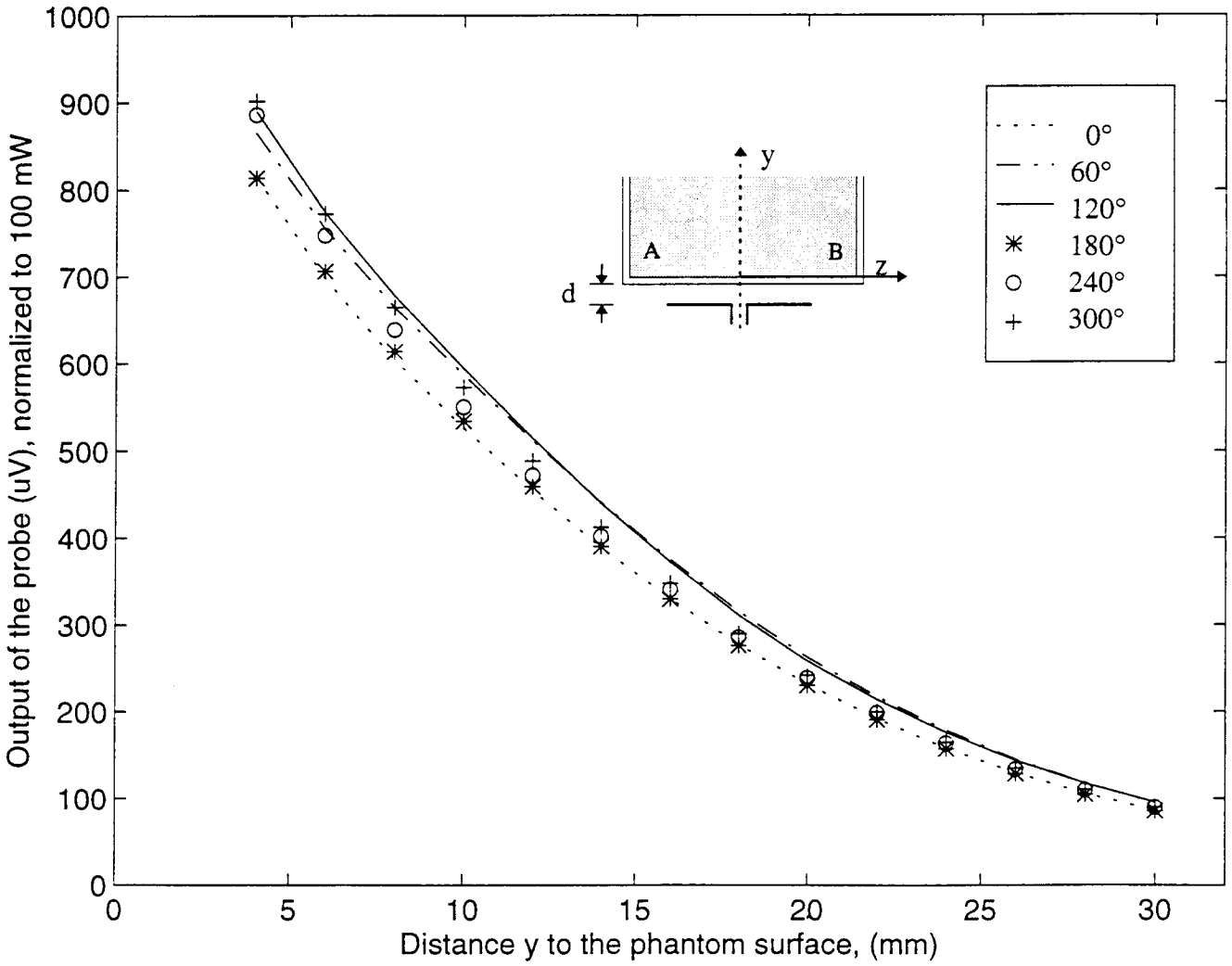

Figure 4a: Test for isotropy: The model shown in Figure 2 was used with nominal half wavelength dipole radiator of length 178 mm at 840 MHz.

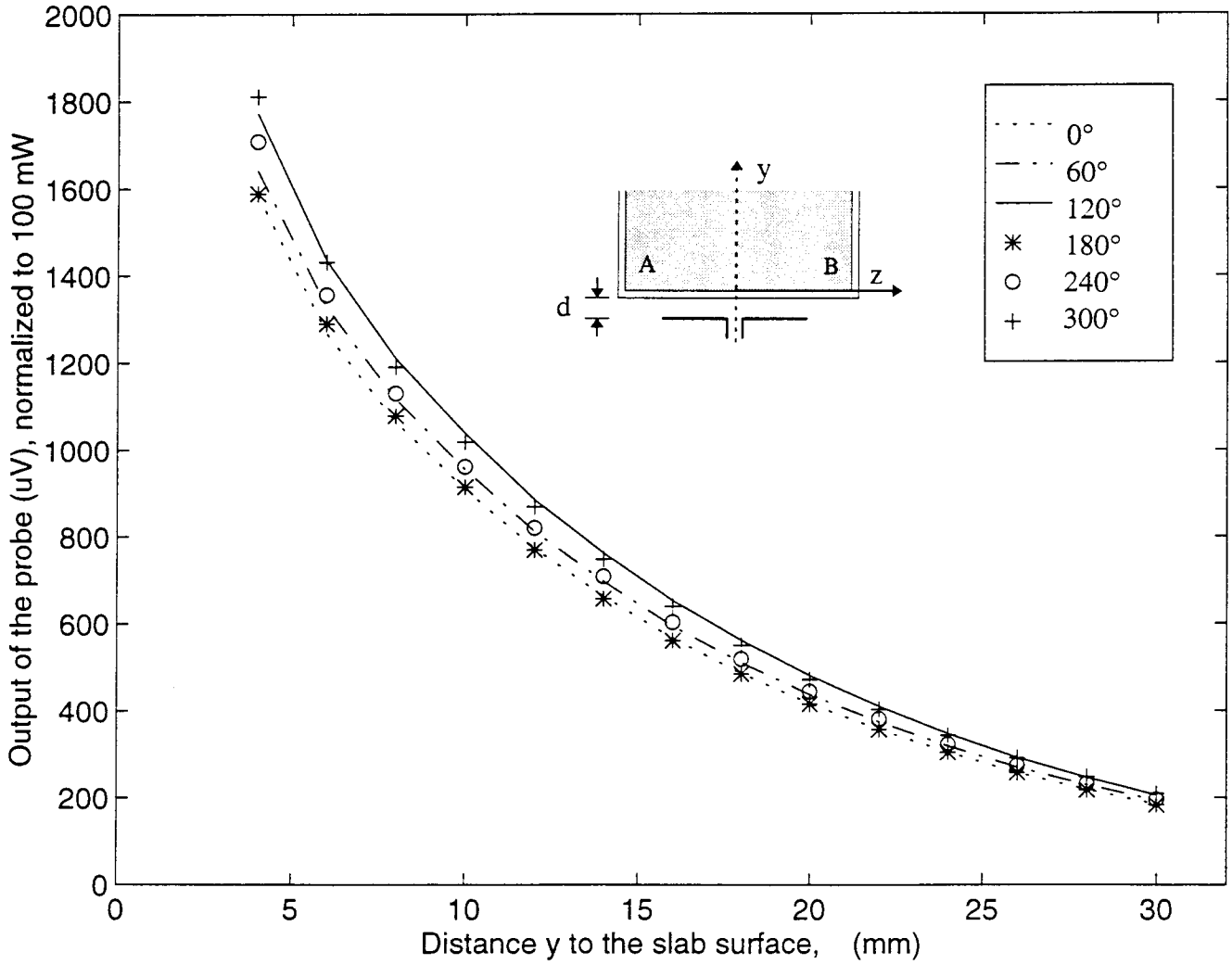

Figure 4b: Test for isotropy: The model shown in Figure 2 was used with nominal half wavelength dipole radiator of length 77 mm at 1900 MHz.

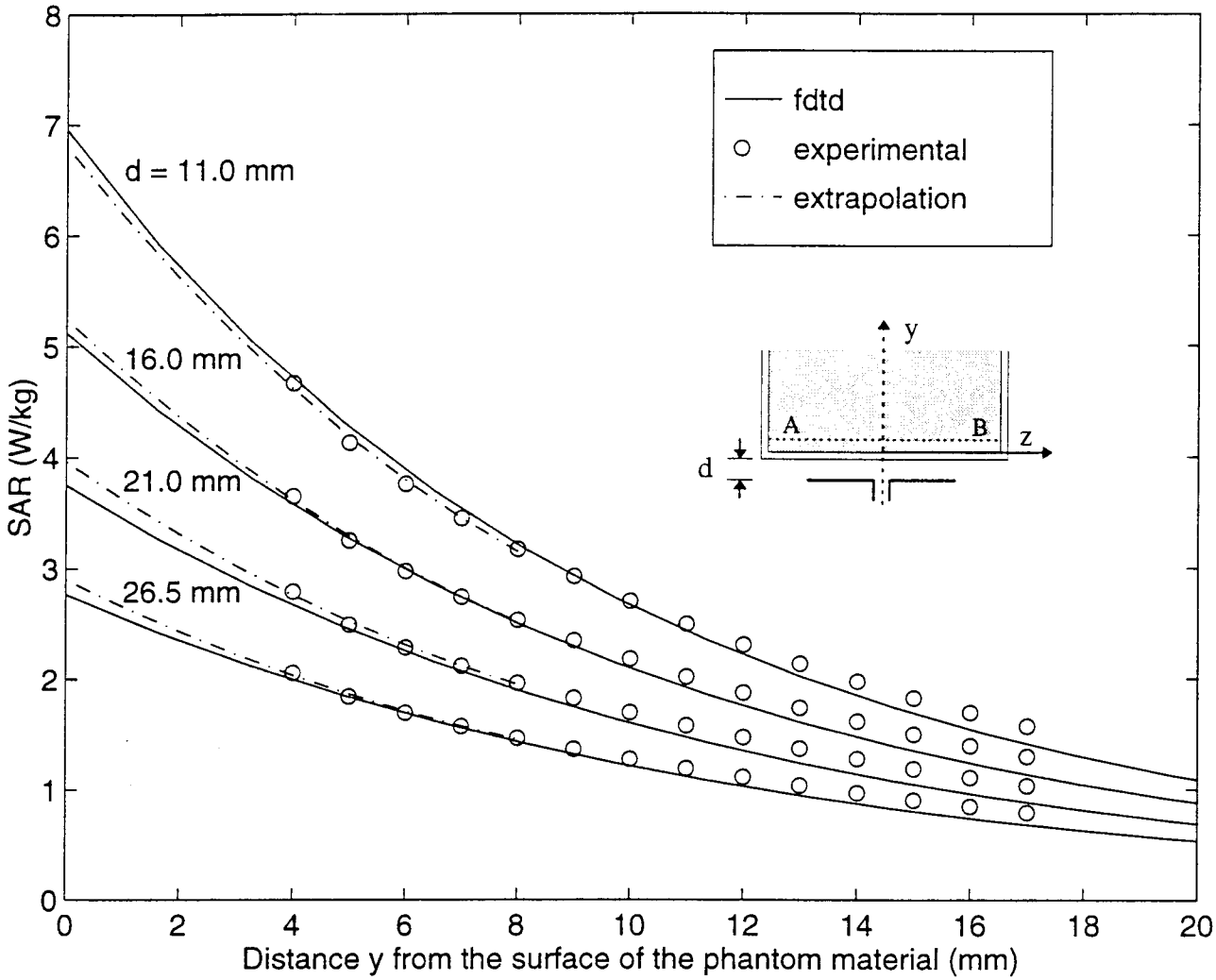

Figure 5a: Comparison of the calculated and measured SAR variations for a box phantom of dimensions 30 x 15 x 50 cm; 840 MHz; $\lambda/2$ dipole antenna; 0.5 W radiated power. Calibration factor for the Narda Model 8021 probe at 840 MHz = 0.49 (mW/kg)/μV. Measured for the phantom material $\varepsilon_r = 41.1$, $\sigma = 1.06$ S/m.

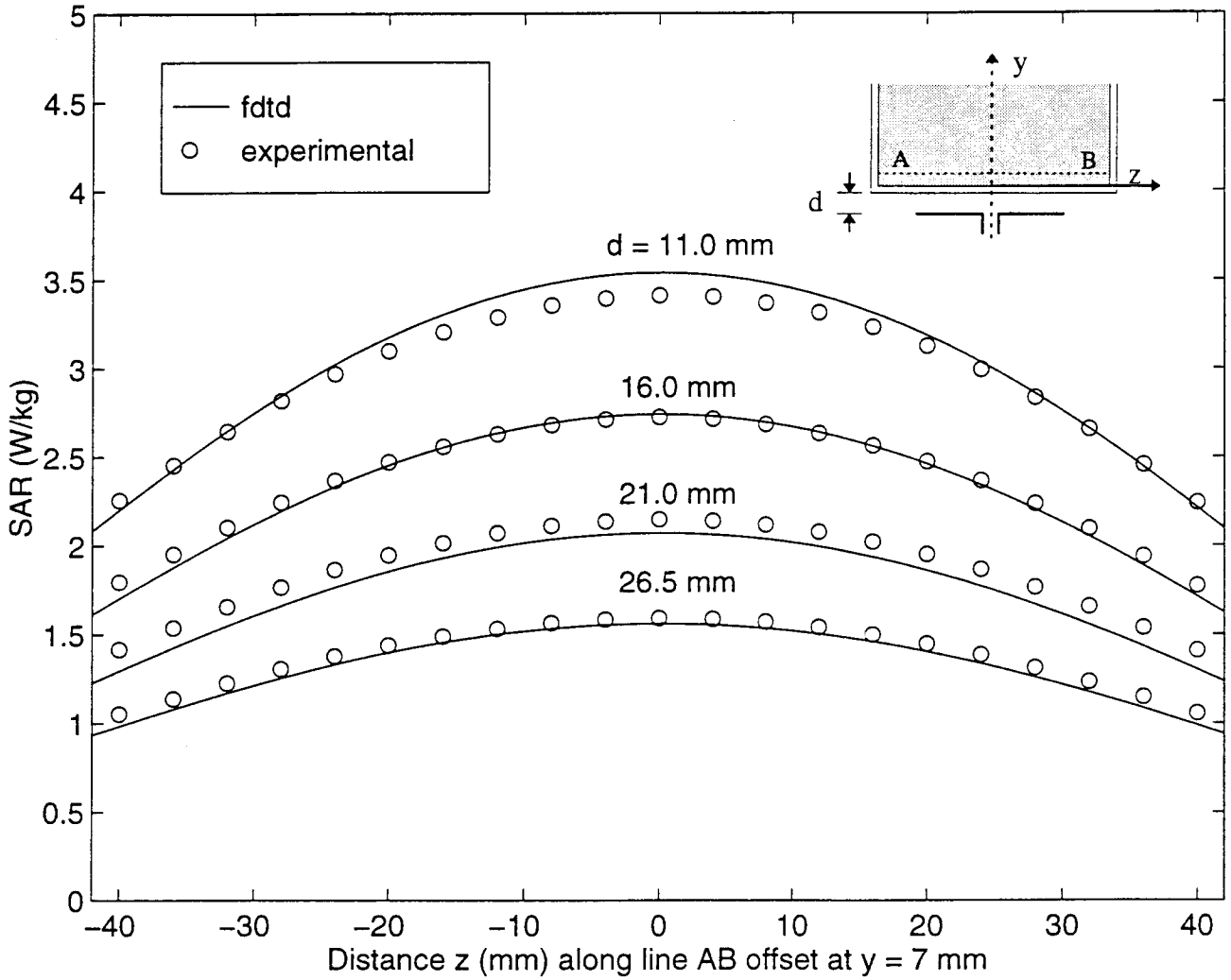

Figure 5b: Comparison of the calculated and measured SAR variations for a box phantom of dimensions 30 x 15 x 50 cm for a line AB parallel to the z axis at a distance y = 7 mm from the surface of the phantom material; 840 MHz; $\lambda/2$ dipole antenna; 0.5 W radiated power. Calibration factor for the Narda Model 8021 probe at 840 MHz = 0.49 (mW/kg)/μV. Measured for the phantom material $\varepsilon_r = 41.1$, $\sigma = 1.06$ S/m.

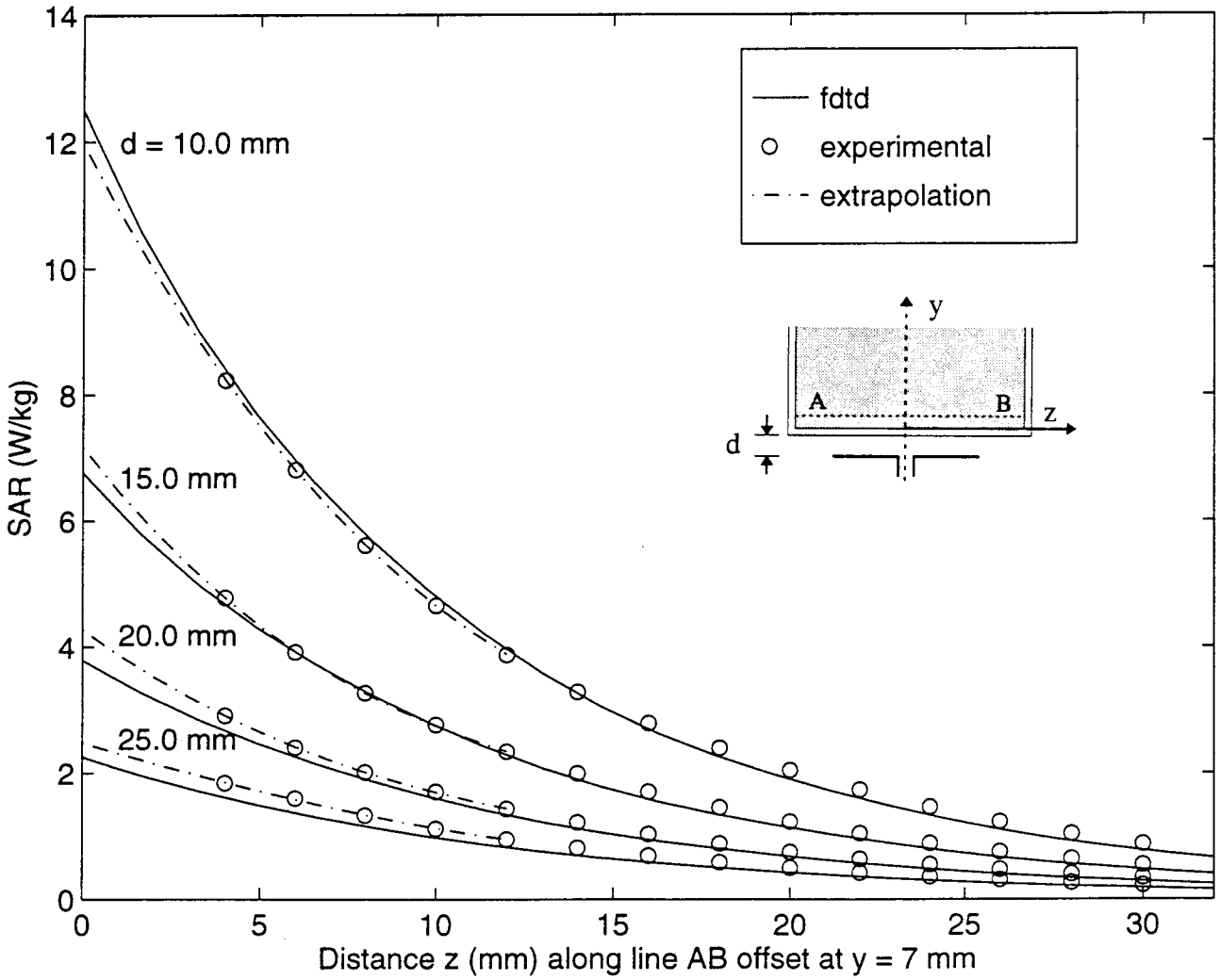

Figure 6a: Comparison of the calculated and measured SAR variations for a box phantom of dimensions 30 x 15 x 50 cm; 1900 MHz; $\lambda/2$ dipole antenna; 0.5 W radiated power. Calibration factor for the Narda Model 8021 probe at 1900 MHz = 0.84 (mW/kg)/μV. Measured for the phantom material $\varepsilon_r = 45.5$, $\sigma = 1.31$ S/m.

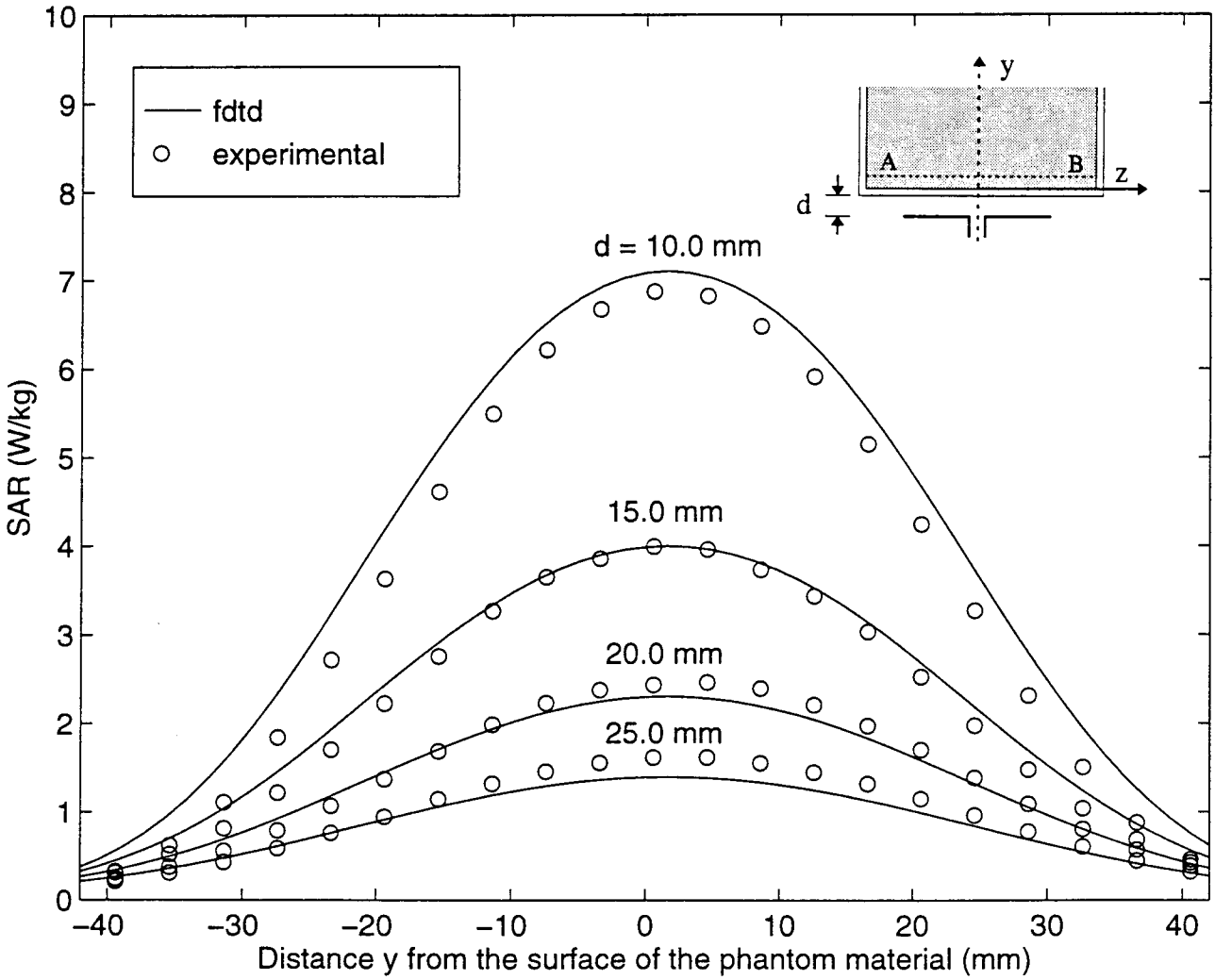

Figure 6b: Comparison of the calculated and measured SAR variations for a box phantom of dimensions 30 x 15 x 50 cm for a line AB parallel to the z axis at a distance y = 7 mm from the surface of the phantom material; 1900 MHz; $\lambda/2$ dipole antenna; 0.5 W radiated power. Calibration factor for the Narda Model 8021 probe at 1900 MHz = 0.84 (mW/kg)/μV. Measured for the phantom material $\varepsilon_r = 45.5$, $\sigma = 1.31$ S/m.

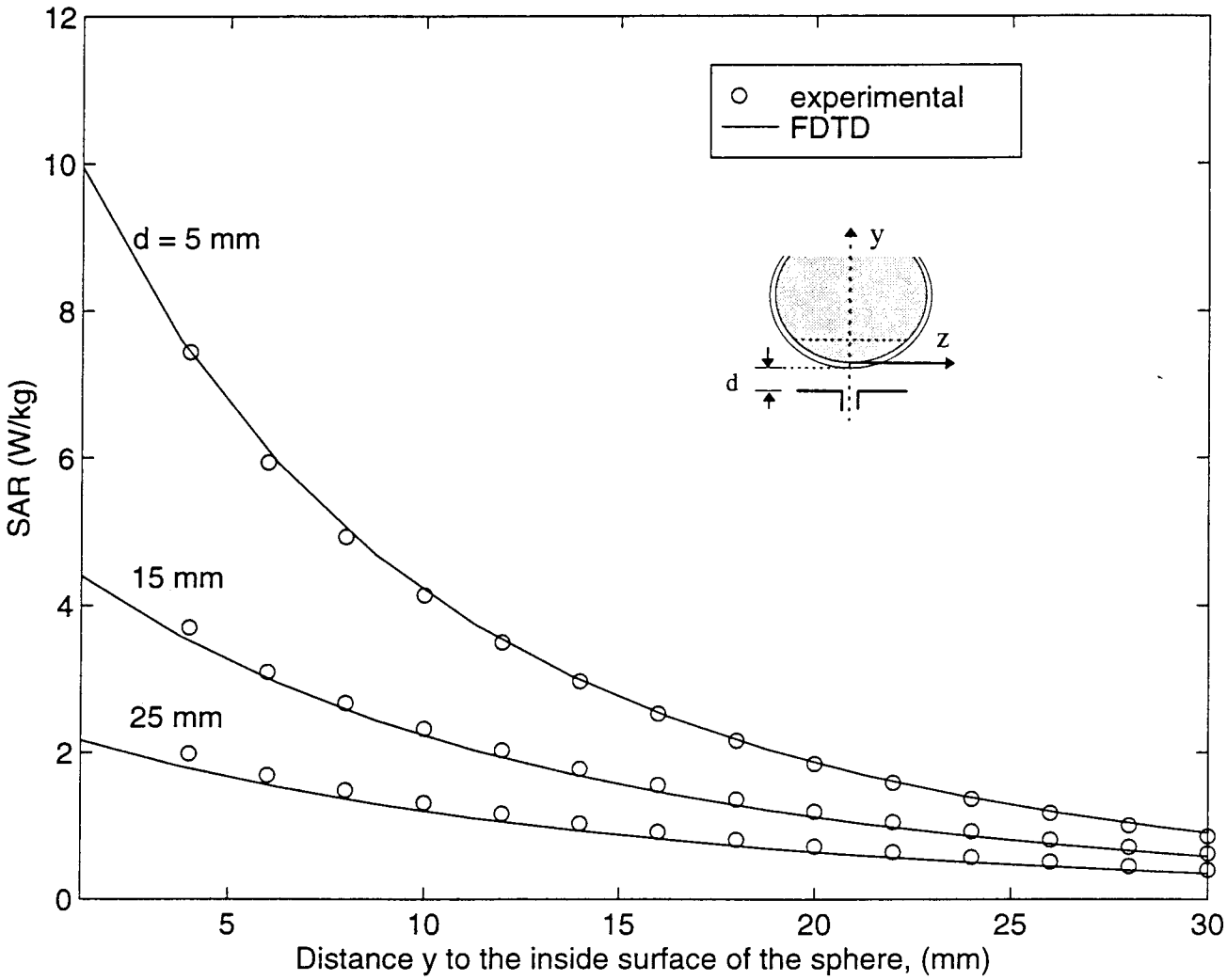

Figure 7a: Comparison of measured and FDTD-calculated SAR variations at 840 MHz for a glass sphere model of outer diameter 22.3 cm and thickness 5 mm. SARs normalized to a radiated power of 0.5 W. Calibration factor = 0.49 (mW/kg)/μV. Measured for the phantom material $\varepsilon_r = 41.1$, $\sigma = 1.06$ S/m.

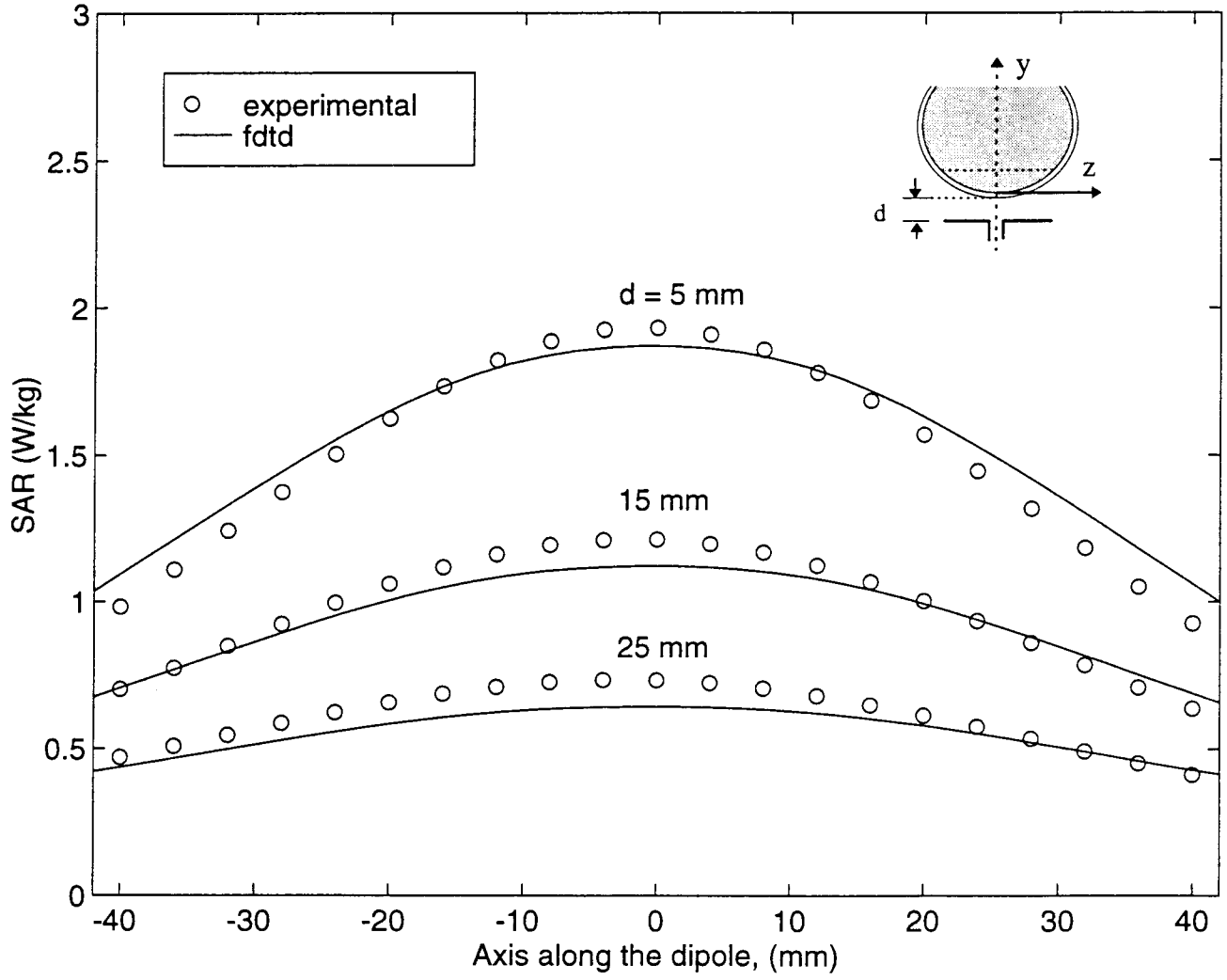

Figure 7b: Comparison of calculated and measured SAR variations at 840 MHz for a plane at a distance of 20 mm from the lowest point on the inside of the sphere. SARs normalized to a radiated power of 0.5 W. Calibration factor = 0.49 (mW/kg)/μV. Measured for the phantom material $\varepsilon_r = 41.1$, $\sigma = 1.06$ S/m.

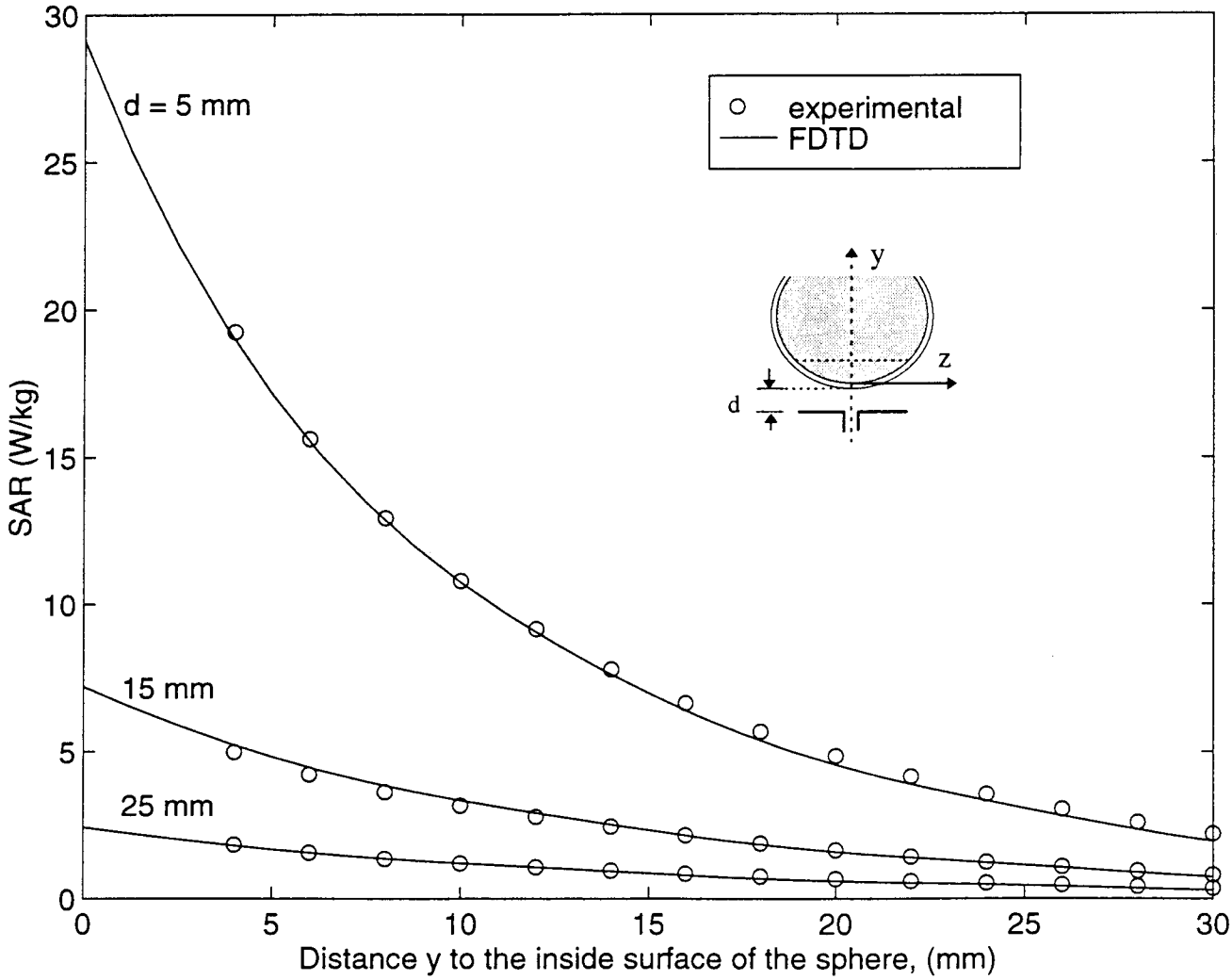

Figure 8a: Comparison of measured and FDTD-calculated SAR variations at 1900 MHz for a glass sphere model of outer diameter 22.3 cm and thickness 5 mm. SARs normalized to a radiated power of 0.5 W. Calibration factor = 0.84 (mW/kg)/μV. Measured for the phantom material $\varepsilon_r = 45.5$, $\sigma = 1.31$ S/m.

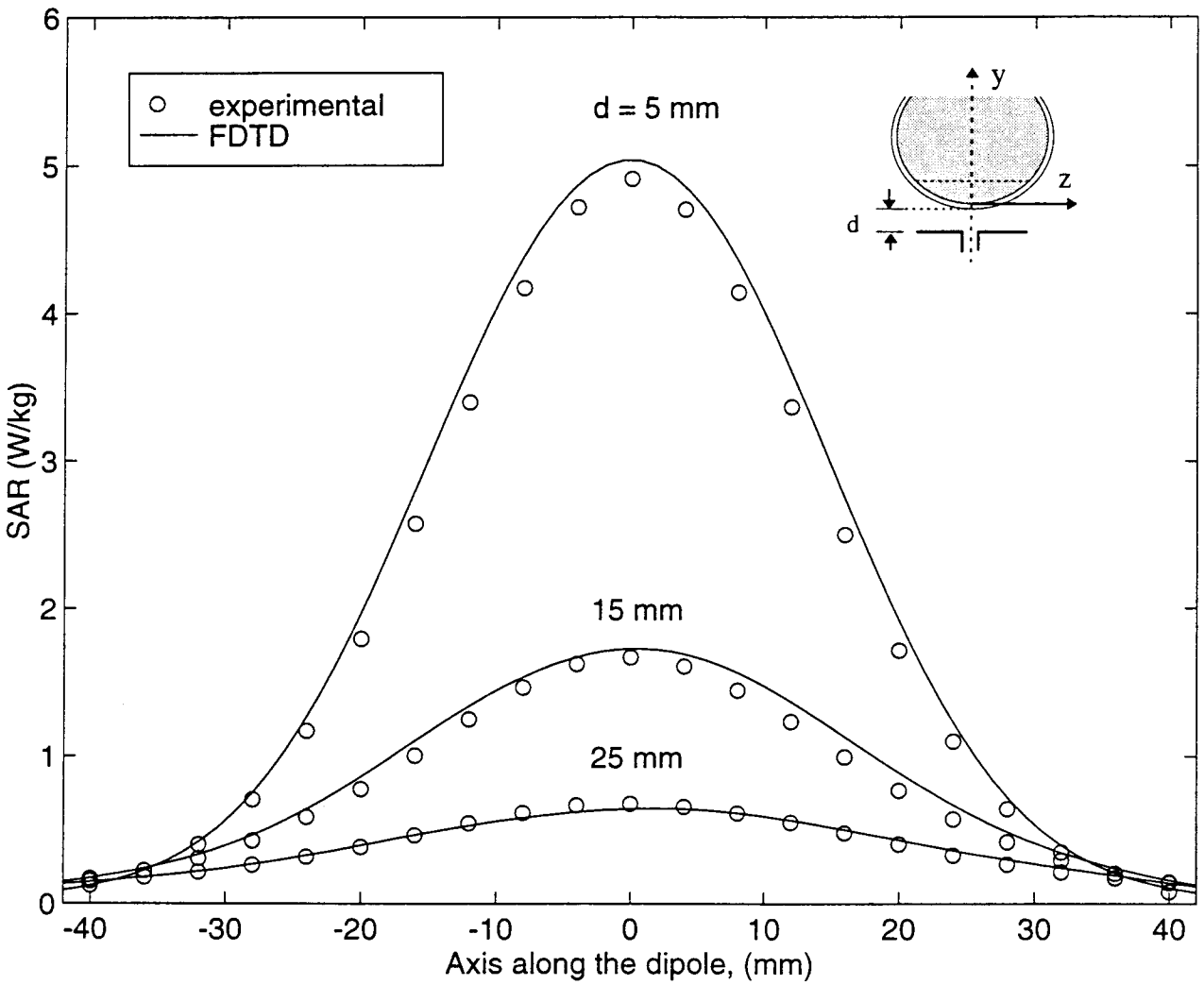

Figure 8b: Comparison of calculated and measured SAR variations at 1900 MHz for a plane at a distance of 20 mm from the lowest point on the inside of the sphere. SARs normalized to a radiated power of 0.5 W. Calibration factor = 0.84 (mW/kg)/μV. Measured for the phantom material $\varepsilon_r = 45.5$, $\sigma = 1.31$ S/m.

Table 1 The desired tissue properties and the measured electrical properties of the tissue-simulant materials used for the phantom model.

	Desired*		Measured	
	ε_r	σ (S/m)	ε_r	σ (S/m)
		840 MHz		
Brain	45.3	0.92	41.1 ± 1.4	1.06 ± 0.05
Skull	17.4	0.25	7.4	0.16
		1900 MHz		
Brain	43.2	1.29	45.5 ± 1.7	1.31 ± 0.06
Skull	16.4	0.45	7.4	0.34

*From C. Gabriel [13]

Table 2 Compositions used for brain-equivalent materials

840 MHz		1900 MHz	
Water	40.4%	Water	60.0%
Sugar	56.0%	Sugar	18.0%
Salt (NaCl)	2.5%	PEP	20.0%
HEC	1.0%	Salt (NaCl)	0.4%
		TX 151	1.6%
$\varepsilon_r = 41.1 \pm 1.4$		$\varepsilon_r = 45.5 \pm 1.7$	
$\sigma = 1.06 \pm 0.05$ S/m		$\sigma = 1.31 \pm 0.06$ S/m	

Table 3 Long Term Stability of the phantom material at 1900 MHz

Day	ε_r	σ (S/m)
1	46.2 ± 1.1	1.35 ± 0.03
7	44.9 ± 1.7	1.29 ± 0.06
15	44.2 ± 1.8	1.25 ± 0.05

Table 4 Box phantom: Comparison of the measured and FDTD-calculated peak 1-g SARs for four spacings each at 840 and 1900 MHz, radiated power normalized to 0.5 W.

Frequency (MHz)	Distance (mm) between λ/2 dipole and the Box	SAR (W/kg) Measured	FDTD	Difference (%)
840	17.5	4.58	4.20	+8.3
840	22.5	3.53	3.65	-3.4
840	27.5	2.69	3.00	-10.2
840	33.0	1.95	2.24	-12.9
1900	16.5	7.45	7.46	-0.1
1900	21.5	4.24	4.18	+1.4
1900	26.5	2.71	2.91	-7.9
1900	31.5	1.77	1.75	+1.1

Table 5 Sphere phantom: Comparison of the measured and FDTD-calculated peak 1-g SARs for three spacings each at 840 and 1900 MHz, radiated power normalized to 0.5 W.

Frequency (MHz)	Distance (mm) between λ/2 dipole and the Box	SAR (W/kg)		Difference (%)
		Measured	FDTD	
840	5	6.78	6.77	+0.23
840	15	3.41	3.27	+4.22
840	25	1.85	1.68	+9.51
1900	5	17.45	18.01	−3.21
1900	15	4.96	5.05	−1.81
1900	25	1.69	1.77	−4.73

Table 6. Comparison of the experimentally measured and FDTD-calculated peak 1-g SARs for ten commercial wireless devices, five each at 835 and 1900 MHz, respectively.

	Time-Averaged Radiated Power mW	Experimental Method W/kg	Numerical Method W/kg
Cellular Telephones at 835 MHz			
Telephone A	600	4.02	3.90
Telephone B	600	5.41	4.55
Telephone C	600	4.48	3.52
Telephone D	600	3.21	2.80
Telephone E	600	0.54	0.53
PCS Telephones at 1900 MHz			
Telephone A	125	1.48	1.47
Telephone B	125	0.13	0.15
Telephone C	125	0.65	0.81
Telephone D	125	1.32	1.56
Telephone E	99.3	1.41	1.25